Giant zero-field cooling exchange-bias-like behavior in antiperovskite $Mn_3Co_{0.61}Mn_{0.39}N$ compound

Ying Sun,[1] Pengwei Hu,[1] Kewen Shi,[1] Hui Wu,[2] Sihao Deng,[1] Qingzhen Huang,[2] Zhiyong Mao,[1] Ping Song,[1] Lei Wang,[1] Weichang Hao,[1] Shenghua Deng,[1] and Cong Wang[1,*]

[1]*Center for Condensed Matter and Materials Physics, Department of Physics, Beihang University, Beijing 100191, People's Republic of China*
[2]*NIST Center for Neutron Research, National Institute of Standards and Technology, Gaithersburg, Maryland 20899–6102, United States*

(Received 12 December 2017; published 25 February 2019)

Giant zero-field cooling exchange-bias-like behavior with $H_{EB} = 3.49$ kOe was found in an antiperovskite $Mn_3Co_{0.61}Mn_{0.39}N$ compound. The magnetic structure of $Mn_3Co_{0.61}Mn_{0.39}N$ was resolved to be ferrimagentic ordering composed of canted Γ^{5g} antiferromagnetic (AFM) and ferromagnetic (FM) along the [111] direction by the neutron diffraction technique. The exchange coupling model was proposed together with the first principles calculation for further understanding this exchange-bias-like behavior. It was found that the ferromagnetic exchange interaction between FM and the canted Γ^{5g} AFM play an important role in the particular exchange-bias-like behavior. The exchange coupling constructed in the lattice is distinct from the interactions between collinear AFM and FM in conventional exchange bias system. In addition to the enhanced horizontal shift, hysteresis loops obtained after FC cooling also exhibited vertical shift. The macroscopic vertical shift of the magnetization is ascribed to the increase of the magnetic moment of canted Γ^{5g} spins along the external magnetic field. This finding will promote the development of advanced magnetic devices.

DOI: 10.1103/PhysRevMaterials.3.024409

I. INTRODUCTION

In recent years, the exchange bias (EB) effect has attracted great attention due to its important application in spintronic devices, ultrahigh-density magnetic recording, and magnetic storage [1,2]. The EB effect means that the magnetic hysteresis loop exhibits a horizontal shift along the magnetic field axis. Generally, the EB effect is attributed to a ferromagnetic (FM) unidirectional anisotropy, which is produced in the field cooling (FC) process since antiferromagnetic (AFM) spins pin FM spins under the external magnetic field due to the interfacial exchange coupling [3]. Interestingly, recent research indicates that the FM unidirectional anisotropy can also be realized under zero-field cooling (ZFC), i.e., ZFC EB behavior. This behavior has been found in Mn_2PtGa [4], $La_{1.5}Sr_{0.5}CoMnO_6$ [5], Ni-Mn-In alloys [6], $YMnO_3$ [7], $Ni_{80}Fe_{20}/Ni_{50}Mn_{50}$ [8], and so on. As ZFC EB behavior does not need an external magnetic field to create the unidirectional anisotropy, it will have broader application than the common EB. Hence, it is worthwhile to explore more materials with ZFC EB behavior.

As a typical strong correlation system, antiperovskite Mn_3XN compounds have recently attracted much attention due to their abnormal physical properties. The observed properties in Mn_3XN compounds almost arise from their special magnetic structures, such as the magnetocaloric [9] and magnetoresistance [10] effects of Mn_3GaC induced by the collinear FM and AFM structure along the (111) direction, the magnetostriction effect of Mn_3CuN [11] induced by ferrimagnetic (FIM) structure (square AFM in the *a*-*b* plane, FM along the *c* axis), negative or near zero thermal expansion of Mn_3Zn_xN [12] and $Mn_3Cu(Ge)N$ [13] induced by the noncolinear Γ^{5g} AFM structure, baromagnetic effects of Mn_3GaN [14] induced by the coexistence of Γ^{5g} AFM and tetragonal FIM structure, and so on. In Mn_3XN, the abundant magnetic properties are contributed by Mn atoms located at face centers since the *X* atom at the corner site and the N atom at the body center are usually nonmagnetic. Once the magnetic element is introduced into the *X* site, the magnetic structure will become more complicated and probably induce more particular behaviors. Especially, it is desirable to obtain a large EB effect for which the coupling effect among spin configurations is necessary. However, this kind of compound with a magnetic element at the *X* site has rarely been investigated in previous work.

Recently, Lin *et al.* [15] have found ZFC EB behavior with the EB field of 510 Oe when partial Mn was introduced into the Ga site of Mn_3GaN. Hence, it is plausible to adjust the spin arrangement by introducing a magnetic element into the corner site in order to obtain the EB effect in antiperovskite compounds. In this work, $Mn_3Co_{0.61}Mn_{0.39}N$ was prepared and the magnetic properties were investigated. It is interesting that the ZFC exchange-bias-like behavior of $Mn_3Co_{0.61}Mn_{0.39}N$ with an EB field larger than 3.49 kOe was observed. Neutron powder diffraction (NPD) experiments were performed to reveal the origin of the large ZFC exchange-bias-like behavior. The results indicate that the coupling interaction between the canted Γ^{5g} AFM and FM spin in the lattice plays a key role in ZFC exchange-bias-like behavior. This type of coupling is abnormal since it is different from the coupling in the conventional EB for which the interaction is between collinear AFM and FM [16] or between spin glass and FM [17], etc.

*Author to who correspondence should be addressed: congwang@buaa.edu.cn

II. EXPERIMENT

The polycrystalline sample in this work was prepared by a solid-state reaction in vacuum using Mn_2N_x, which was synthesized by sintering Mn powder (99.9%) in a nitrogen flow at 750 °C for 48 h, and Co with a purity of 99.99% as raw materials. Stoichiometric amounts of the starting materials were mixed, ground for 1 h and pressed into pellets. The pellets were wrapped in Ta foil and then sealed in an evacuated quartz tube. The quartz tube was heated at 800 °C for 80 h in a box furnace and allowed to cool naturally to room temperature.

The x-ray diffraction (XRD) pattern of this sample was obtained from an X'pert PRO powder diffractometer using Cu kα radiation at room temperature. Temperature dependent magnetization $M(T)$ from 10 to 350 K and magnetic hysteresis loops $M(H)$ between −90 and 90 (kOe) at 10 K were measured by a superconducting quantum interference device. The NPD experiments were performed at the National Institute of Standards and Technology Center for Neutron Research on the BT-1 high-resolution neutron powder diffractometer using a Cu (311) monochromator with wavelength of 1.5403 Å. Neutron diffraction data was collected at various temperatures in the range of 5–320 K. The crystal and magnetic structures were determined by the Rietveld refinement method with the software of General Structure Analysis System. The neutron scattering amplitudes used in refinements were −0.373, 0.249, and 0.936 ($\times 10^{-12}$ cm) for Mn, Co, and N, respectively.

III. RESULTS AND DISCUSSION

The XRD pattern at room temperature was first collected to determine the crystal structure of the as-prepared sample, as shown in Fig. 1(a). The Rietveld refinement results reveal that the crystal structure is cubic with space group $Pm\bar{3}m$ (shown in the inset of Fig. 1) and the details of the structural parameters are listed in the Supplemental Material [18]. Additionally, a small amount of extra MnO and Co was detected in this sample. The total occupancies at the corner and face center sites for $Mn_3Co_{0.61}Mn_{0.39}N$ were confirmed to be 100%. However, the occupancies of N and the respective occupancies of Mn and Co at corner site could not be defined by XRD due to the light N and the close x-ray scattering factors of Mn and Co. Hence, the NPD pattern was measured and the occupancies of N, Mn, and Co at the corner and face center are determined using the Rietveld refinement. Based on the result, the compound was finally defined as $Mn_3Co_{0.61}Mn_{0.39}N$. Details of the refinement (shown in Fig. 3) will be discussed later.

The magnetic hysteresis loops were collected at 10 K in the protocol (P type) : (+90 kOe) → 0 → (−90 kOe) → 0 → (+90 kOe), after cooling from 300 K without applying the magnetic field. As shown in Fig. 2(a), a large horizontal shift of the loops along the field axis was found, indicating the appearance of ZFC exchange-bias-like effect. The EB field is generally defined as $H_{EB} = |H_L + H_R|/2$, and coercivity is defined as $H_C = |H_L - H_R|/2$, in which H_L and H_R are coercivity at the negative and positive magnetic field axis, respectively. The H_{EB} and H_C are calculated to be 3.49 and 9.75 kOe, respectively. To confirm the occurrence of ZFC exchange-bias-like behavior, the ZFC magnetic hysteresis loops were further measured at 10 K in the protocol (N type) : (−90 kOe) → 0 → (+90 kOe) → 0 → (−90 kOe). The horizontal shift of the loops still exists and the H_{EB} of the N-type magnetic hysteresis loop is determined to be 3.32 kOe, which is close to the value for P type. The symmetry of P-type and N-type loops in Fig. 2(a) implies that the EB in this sample is intrinsic, but not induced by remnant magnetization.

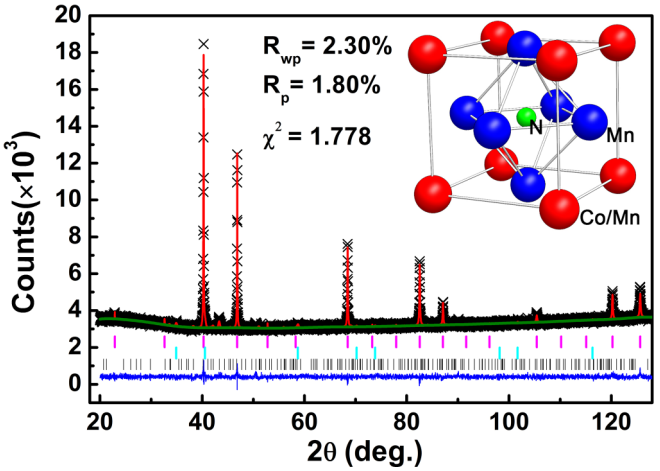

FIG. 1. Rietveld refinement analysis of XRD pattern recorded at room temperature. In (a), the crosses signify the experimental intensities; the solid red and green lines show the calculated pattern and background, respectively; the blue line means the difference between experimental and calculated intensities. The vertical bars with the colors of pink, cyan, and black show the Bragg reflections of $Mn_3Co_{0.61}Mn_{0.39}N$, MnO, and hexagonal Co alloy, respectively. (b) shows the crystal structures of $Mn_3Co_{0.61}Mn_{0.39}N$. *Note:* R_{wp} means the weighted residual variance between the refined and measured data, R_p means the residual variance between the refined and measured data, and χ^2 means the goodness of fit.

Further, the hysteresis loops with different cooling magnetic fields were measured. As shown in Fig. 2(b), the EB field of these FC loops are obviously larger than that of the ZFC loops, i.e., horizontal shifts are enhanced after FC. In addition to horizontal shifts, it is noteworthy that these FC loops also show a vertical shift toward the positive direction. The vertical shift is defined as $M_{EB} = |M_U + M_D|/2$, where M_U and M_D are the positive and negative remnant magnetizations, respectively. Exchange-bias field H_{EB}, coercivity H_C and magnetization shift M_{EB} calculated from Figs. 2(a) and 2(b) are shown in Fig. 2(c) as a function of cooling field H_{FC}. It was found that H_{EB}, H_C, and M_{EB} increase with increasing cooling field, especially when the cooling field increases from 0 to 10 kOe. However, after the cooling field increases to 30 kOe, these behaviors become nearly saturated. The observed maximum values for H_{EB}, H_C, and M_{EB} are 9.56 kOe, 19.37 kOe and 1.14 emu/g, respectively. In the case of the ZFC loop, M_{EB} for both P type and N type are 0.004 μ_B/f.u., which are much smaller than that of FC loops. Therefore, the large vertical shift can be attributed to the FC effect. Further, it was found that the cooling magnetic field dependence of M_{EB} could be well fitted using a simplified exchange interaction model as

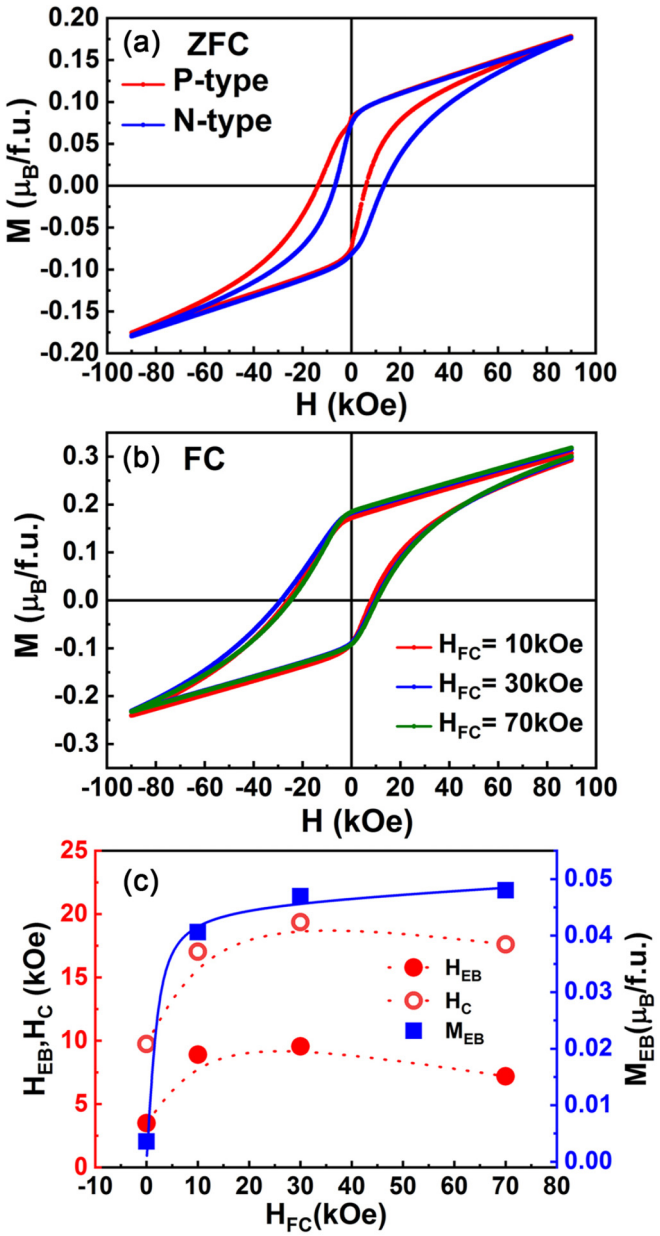

FIG. 2. (a) Zero-field-cooled (ZFC) $M(H)$ loops of P type and N type measured at 10 K. (b) Field-cooled (FC) $M(H)$ loops of P type after field cooling in $H_{FC} = 10$, 30, and 70 kOe, respectively. (c) Cooling field dependence of exchange-bias field H_{EB}, coercivity H_C, and magnetization shift M_E calculated from (b). The dotted lines are guides to the eyes and the solid line is the fitting result of the cooling external magnetic field dependence of M_{EB}.

follows: $M_{EB} \propto J_i[\frac{J_i u_0}{(g u_B)^2} L(\frac{u H_{cool}}{k_B T_f}) + H_{cool}]$, where J_i represents the interface exchange constant $J_{Mn\text{-}Co}$ between Mn at the face center and Co/Mn at the corner, g is the Lande factor, μ_B is the Bohr magneton, $L(x)$ is the Langevin function, μ_0 is the vacuum permeability, and k_B is the Boltzmann constant [19]. The fitting result was shown in Fig. 2(c) and the exchanged integral constant $J_{Mn\text{-}Co}$ was determined to be 1.17 meV. The positive value of $J_{Mn\text{-}Co}$ indicates that the EB behavior arises from the ferromagnetic exchange interaction.

Spin arrangement is crucial to clarify the abnormal exchange-bias-like behavior. Hence, neutron diffraction data was collected and used to resolve the magnetic structure by the Rietveld refinement method. From Fig. 3(a), it can be clearly seen that the calculated peak intensities are significantly lower than the observed one when only nuclear peak fitting was applied. The differences between observed and calculated intensities such as (101), (110), and (211) peaks should be from the contribution of the magnetic phase. Then, the magnetic structure model would be constructed for Rietveld refinement. From the diffraction peak of the neutron diffraction pattern, we can determine that the propagation vector $\mathbf{k}$ should be $\mathbf{k} = (0, 0, 0)$. According to $\mathbf{k} = (0, 0, 0)$, the types of magnetic structure includes R-3m, R-3m', $Cmm'm'$, $P4/mm'm'$, $P4'/mm'm$, etc. [20]. Rietveld refinements have been carried out using the above structure and the FM component on the Co/Mn atom located at the corner site was also considered. The refinement results for all of the above magnetic structures are shown in the Supplemental Material [18]. Among those, we screened out the best magnetic model depending on the refinement rules (higher symmetry, less parameters, goodness of fitting). It was found that the best magnetic model is the maximum magnetic rhombohedral subgroup R-3m within the irreducible magnetic representation Γ^{5g}, for which three nearest-neighbor Mn spins in the (111) plane are arranged by a 120° rotation from the neighboring spins in either clockwise or counterclockwise configuration [21]. The refinement factors for the previous magnetic model were $R_{wp} = 6.76\%$, $R_p = 6.29\%$, and $\chi^2 = 1.076$, respectively. Further, it was found that a better fitting result could be achieved when the Γ^{5g} was considered to be canted, since all of the above factors decreased to $R_{wp} = 6.53\%$, $R_p = 5.85\%$, and $\chi^2 = 1.047$. Finally, the best fit could be obtained using the magnetic structure model shown in Fig. 3(d). It can be seen that the canted Γ^{5g} phase means that Mn spins rotate from the (111) plane. Thus, there is a FM component perpendicular to the (111) plane for Mn spins at the face center, which is parallel to FM spin along [111] for Co/Mn spins at the corner. The difference between the calculated data of Figs. 3(a) and 3(b) was shown in Fig. 3(c), which reflected the magnetic contribution of $Mn_3Co_{0.61}Mn_{0.39}N$. Details of the refined parameters are listed in Table I. In this work, the occurrence of the canting of Γ^{5g} probably arises from the chemical strain effect. In Ref. [22], the calculation results have shown that the strain effect in Mn_3GaN and Mn_3ZnN introduced by decreasing the lattice constant can cause the Mn spins at the face center to rotate from the triangular Γ^{5g} structure and induce uncompensated spin. In this work, the lattice constant of $Mn_3Co_{0.61}Mn_{0.39}N$ is $a = 3.87116(4)$ Å, which is obviously smaller than the other Γ^{5g} phase, such as Mn_3GaN (~3.899 Å) and Mn_3ZnN (~3.901 Å) [12,23]. Thus, the chemical strain may exist and it is correlated to the canting of Γ^{5g} spins.

According to the neutron diffraction data, the temperature dependence of FM (Mn/Co at corner) and AFM (Mn in Γ^{5g}) moments from 5 to 300 K are obtained as shown in Fig. 4. It can be observed that both FM moments and AFM moments disappear near 260 K. This reveals that the ordered FM and Γ^{5g} AFM magnetic sublattices are established simultaneously by spontaneous magnetization. The synchronicity

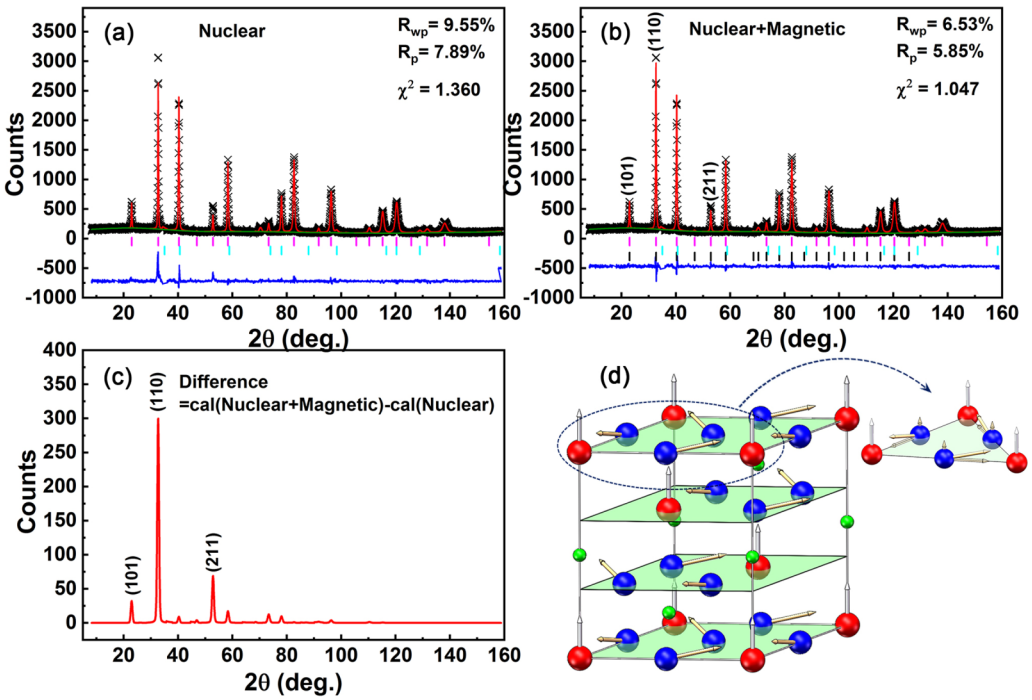

FIG. 3. NPD pattern recorded at 5 K. In (a) and (b), the crosses signify the experimental intensities; the solid green and red lines show the calculated pattern of background and peaks, respectively; the blue line means the difference between experimental and calculated intensities. The vertical bars with the colors of pink and cyan show the Bragg reflections of $Mn_3Co_{0.61}Mn_{0.39}N$ and MnO, respectively. The black vertical bars in (b) show Bragg reflections in the $Mn_3Co_{0.61}Mn_{0.39}N$ magnetic structure. (c) indicates the difference between the calculated data of (a) and (b), which is generated by magnetic contribution of $Mn_3Co_{0.61}Mn_{0.39}N$. (d) shows the magnetic structure of $Mn_3Co_{0.61}Mn_{0.39}N$, in which the white arrows in the direction of [111] indicate FM spins on the corner atoms in the cubic structure, and the golden arrows indicate canted Γ^{5g} AFM spin structure.

of FM and AFM spins will result in the formation of the exchange coupling interaction in the cooling process without applying the magnetic field. On the other hand, the refined AFM moment for Mn is 1.43(1) μ_B and the average moment of FM spins at the corner (Mn and Co) is 1.25(9) μ_B at 5 K. The magnetic moment is much smaller than those observed in other systems. For example, the FM moment for $Mn_3Ni_{0.667}Mn_{0.333}N$ is about 3.1 μ_B/Mn atom, nearly 2.5 times of that for $Mn_3Co_{0.61}Mn_{0.39}N$ [24]. The much smaller FM moment indicates a strong itinerant electron character of $Mn_3Co_{0.61}Mn_{0.39}N$. In Mn_3XN, narrow bands are formed near the Fermi level by the strong hybridation between N 2*p* and Mn 3*d* orbitals. The occupation of these narrow bands is sensitively changed according to the choice of the *X* atom. Itinerant magnetism largely depends on the electronic density of states at the Fermi level E_F, which is sensitive to the choice of the *X* atom. Commonly, the magnetic moment in this type of antiperovskite compound will be affected by the lattice constant (i.e., the bond length of Mn-N) and the number of valence electrons of the *X* atom at the corner site [21]. Compared with $Mn_3Ni_{0.667}Mn_{0.333}N$, $Mn_3Co_{0.61}Mn_{0.39}N$ has a smaller lattice constant and a lower number of valence electrons. No matter which one we consider, they would enhance the N_{2p}–Mn_{3d} hybridization and broaden the

TABLE I. Rietveld refinement results of the NPD pattern for the $Mn_3Co_{0.61}Mn_{0.39}N$ compound. The space group for the nuclear structure is *Pm*-3*m* (No. 221), $Z = 1$, $a = 3.86661(5)$ Å, and $V = 57.808(2)$ Å^3. The space group for the magnetic structure is *R*-3 (No. 148). *R* factors were $R_{wp} = 6.53\%$ and $R_p = 5.85\%$. In this table, the Wyckoff position is a point belonging to a set of points for which site symmetry groups are conjugate subgroups of the space group, *g* is the occupancy factor, *x*, *y*, *z* mean the atomic coordinates. *B* (Biso) is the isotropic displacement parameter. $M_\parallel$ is the magnetic moment in the (111) plane, while $M_\perp$ is the moment of FM component perpendicular to the (111) plane for Mn spins at the face center.

Atom	Wyckoff position	*G*	*x*	*y*	*z*	*B*(Å^2)	Moment (μ_B)
N	1b	1	0.5	0.5	0.5	0.27(3)	–
Co	1a	0.610(4)	0	0	0	1	1.79(7)
Mn1	3c	1	0.5	0.5	0	0.29(3)	1.43(5)
							$M_\parallel$: 1.41(4) $M_\perp$: 0.21(7)
Mn2	1a	0.390(4)	0	0	0	1	1.79(7)

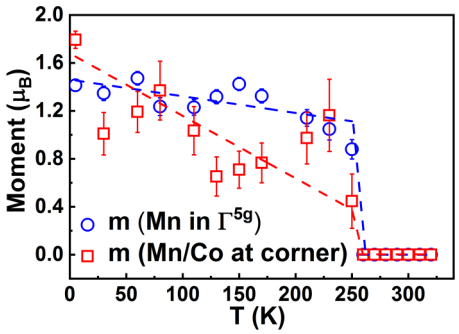

FIG. 4. Temperature dependence of FM and AFM moments from 5 to 300 K. The lines are guides to the eyes.

electronic band, thus N (E_F) reduces and magnetic moment decreases.

Next, we will focus on a discussion about ZFC exchange-bias-like behavior. In the zero-field cooling process, the FM or AFM spins of each grain is random when the magnetic structure forms as the temperature decreases below the transition temperature. After applying the magnetic field in the initial magnetizing process, both the FM and canted AFM spins tend to align along the direction of magnetic field. However, in this system, there exists a coupling effect between canted Γ^{5g} AFM and FM, magnetic frustration, and large anisotropy of Γ^{5g} AFM. The complex interactions and polycrystalline do not allow the spins to exactly align along the magnetic field direction. Thus, when the initial magnetization process increases to the maximum magnetic field ($+H_{max}$ = 90 kOe), the spins should be partially ordered, as shown in Fig. 5(a). It is worth mentioning that the system will reach a metastable state after the initial magnetization process and the establishment of the above spin arrangement would be irreversible. In addition, it should be noted the spontaneous ferromagnetic exchange interaction between FM along [111] and the FM component of canted Γ^{5g} AFM spins remains. The ferromagnetic exchange interaction has been characterized by the positive exchanged integral constant $J_{Mn\text{-}Co}$ (1.17 meV) as discussed above.

The schematic of spin rotation in the process of ZFC hysteresis loop (P-type) was shown in Fig. 5(c). With decreasing magnetic field from $+H_{max}$ to an opposite field, FM spins of Co/Mn at the corner site will rotate together with the external magnetic field. Based on the discussion in Ref. [25], it was proposed that $K_{AFM} \geqslant J_{INT}$ is required for the observation of EB behavior, where K_{AFM} is the anisotropy of the AFM spin and J_{INT} is the interface coupling constant. On the contrary, if $J_{INT} \gg K_{AFM}$, AFM and FM spins will rotate together. In this work, the exchanged integral constant $J_{Mn\text{-}Co}$ (1.17 meV) is apparently smaller than K_{AFM} of Γ^{5g}, which has been evaluated to be about 2.8 meV [26]. Therefore, it is hard for Γ^{5g} to rotate with FM spins under external magnetic field and the ferromagnetic exchange interaction between FM spins and Γ^{5g} spins will hinder the reversal of FM spins. In this process, additional interaction coupling energy between the AFM and FM spins may also be induced. Consequently, the external magnetic field required to completely reverse the magnetization in the FM will be higher than the case where the FM is not coupled to an AFM. An exchange coupled model was

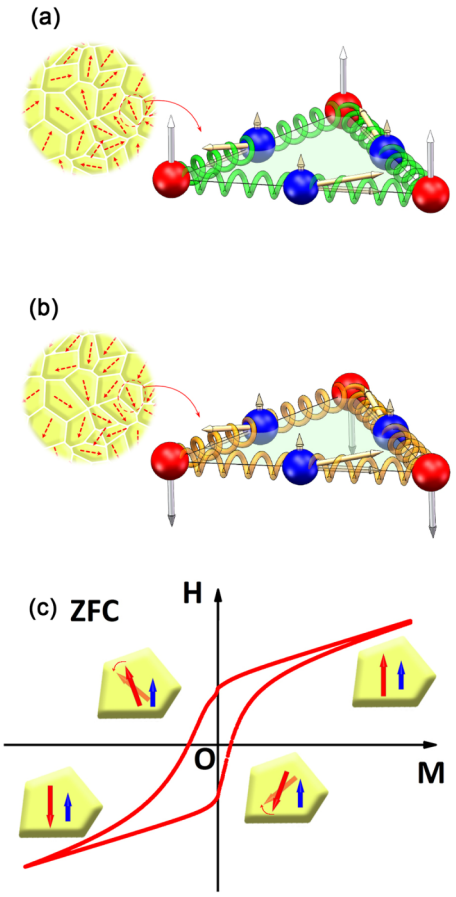

FIG. 5. (a) and (b) are schematics of the exchange coupling interaction between canted Γ^{5g} AFM spins and FM spins at $+H_{max}$ and $-H_{max}$, respectively. (c) is the schematic of spin rotation in the magnetization process of the ZFC hysteresis loop, the red arrows indicates FM spins for Co/Mn at the corner, while the blue arrows indicate the FM component along [111] for Mn spins at the face center.

proposed to understand this ZFC exchange-bias-like behavior. The right part of Figs. 5(a) and 5(b) shows the spin orientation at $+H_{max}$ and $-H_{max}$, respectively. As shown in Fig. 5(a), green springs indicate that the exchange coupling energy between the FM and canted Γ^{5g} AFM spins is low at $+H_{max}$ after the initial magnetization process. On the other hand, orange springs in Fig. 5(b) indicate the induced high coupling energy at $-H_{max}$. If the magnetic field is further reversed back to the positive branch from $-H_{max}$, the high coupling energy between FM and AFM spins will favor the magnetization reversal, and the rotation of spins in the FM will be easier than that in an uncoupled FM. Therefore, the coercive field in the positive field branch will be reduced and a horizontal shift of the $M(H)$ curves to a negative direction was observed in the whole process.

To check the availability of the above proposed model, we performed the first principles calculation to deeply understand the mechanism of the abnormal ZFC exchange-bias-like effect. The computational structure model consists of $2 \times 2 \times 2$ $Mn_3Mn_{0.5}Co_{0.5}N$ formula units including 40 atoms (shown in the Supplemental Material [18]), i.e., $Mn_{24}Mn_4Co_4N_8$. All

the calculations of the $Mn_3Mn_{0.5}Co_{0.5}N$ are implemented in the Vienna *ab initio* simulation package (VASP) code with the projector augmented wave approach. The generalized gradient approximation of the framework of the density functional theory is used, with the exchange-correlation functional following the approach of Perdew-Burke-Ernzerhof) for unconstrained noncollinear magnetic structures. We perform $3 \times 3 \times 3$ k-point sampling and the Methfessel-Paxton integration method and describe the electronic wave functions by a set of plane wave functions with the energy cutoff of 400 eV to be sufficient to achieve a total energy convergence. The total energy was calculated based on the structure parameters and magnetic moments resolved from Rietveld refinement of the NPD data. The total energy according to the model in Fig. 5(a) is -51.860 eV/unit cell whereas it is -51.814 eV/unit cell for the model in Fig. 5(b). Hence, the total energy at $-H_{max}$ is higher than that at $+H_{max}$ and the energy difference with 46 meV/unit cell is enough to induce the EB effect. The calculation results proved that the above proposed model is reasonable and the ferromagnetic component from the triangular Γ^{5g} structure plays an important role in the abnormal ZFC EB behavior. As reported earlier, most EB models are ascribed to the collinear AFM-FM spins at the interface. This work reveals experimentally that it is not a necessary condition. The ZFC exchange-bias-like behavior observed in this work is closely related to the exchange coupling interaction between the FM and canted AFM spins. Different from the common systems, the exchange coupling interaction in $Mn_3Co_{0.61}Mn_{0.39}N$ is not at the interface but exists throughout the lattices, which may be the reason for the relatively large H_{EB}.

For M-H curves, another worthy result is the shift of hysteresis loops along the vertical axis and the increase of the EB field after the FC process. Since the *M-H* curves are nonsquare, we first calculated the vertical shift M_{EB} induced by the horizontal shift according to the formula: $M_{EB} = (\chi(H=0)^+ + \chi(H=0)^-) \times H_{EB}$, where $\chi(H=0)^+$ and $\chi(H=0)^-$ are the slope of the $M(H)$ curve for an upward and downward field sweep, respectively. The results are about 0.026, 0.028, and 0.021 μ_B/f.u. with the cooling field of 10, 30, and 70 kOe, respectively. The values are obviously smaller than the observed vertical shift (0.041, 0.047, 0.048 μ_B/f.u.). Thus, the vertical shift of the magnetization was not only induced by the horizontal shift but also for another reason. In fact, based on the exchange model clarified in Fig. 5, the vertical shift should be expected due to the FM component of canted Γ^{5g}. However, in the ZFC magnetization curves, the vertical shift induced by the macroscopic magnetic moment of the FM component is not large enough to be observed since the ferromagnetic coupled spins are partially ordered along the magnetic field direction. As we know, the FC effect on the spin arrangement will be much more prominent than the initial magnetization process after ZFC. Thus, if an external field is applied during the cooling process, it will promote more spins aligning towards the direction of the applied field. This will result in the increase of the ferromagnetic moment and thereby strengthen the ferromagnetic exchange interaction between FM and canted AFM spins. The above effects play an important role in the increase of the vertical shift and EB field after the FC process, which is clearly seen in Fig. 2(c). The presence of vertical shift accompanied with the EB has also been associated with the presence of uncompensated spins pinned at the interface, such as in CoO/NiFe [27], CoO/Cu [28], $Pt/Co/Cr_2O_3$ [29], IrMn/CoFeB [30], etc.

IV. CONCLUSION

In conclusion, giant ZFC exchange-bias-like behavior larger than 3.49 kOe was found in $Mn_3Co_{0.61}Mn_{0.39}N$. The magnetic structure of $Mn_3Co_{0.61}Mn_{0.39}N$ was resolved to be a FIM ordering composed of canted Γ^{5g} AFM in the (111) plane and FM perpendicular to the(111) plane by the neutron diffraction method. It was proposed that the ferromagnetic coupling between the FM and canted Γ^{5g} constructed in the lattice plays an important role in the ZFC exchange-bias-like behavior, which was also supported by the results from the first principles calculation. Furthermore, it was found that the FC process induced the larger EB field and vertical shifts due to both the enhancement of the magnetic moment along the magnetic field and ferromagnetic exchange interaction between FM and canted AFM spins. This study launches a potential candidate for the ZFC EB effect that could have important application in advanced magnetic devices.

ACKNOWLEDGMENTS

The authors acknowledge the support of the Steady High Magnetic Field Facilities (SHMFF) at High Magnetic Field Laboratory, Chinese Academy of Science. This work is financially supported by the National Natural Science Foundation of China (NSFC) (Grants No. 51472017, No. 51732001, and No. 51572010), the Fundamental Research Funds for the Central Universities, and the Aeronautical Science Foundation of China.

[1] S. Gider, B. U. Runge, A. Marley, and S. Parkin, Science **281**, 797 (1998).
[2] D. Suess, T. Schrefl, S. Fähler, M. Kirschner, G. Hrkac, F. Dorfbauer, and J. Fidler, Appl. Phys. Lett. **87**, 012504 (2005).
[3] S. Giri, M. Patra, and S. Majumdar, J. Phys.: Condens. Matter. **23**, 073201 (2011).
[4] A. K. Nayak, M. Nicklas, S. Chadov, C. Shekhar, Y. Skourski, J. Winterlik, and C. Felser, Phys. Rev. Lett. **110**, 127204 (2013).
[5] J. Krishna Murthy and A. Venimadhav, Appl. Phys. Lett. **103**, 252410 (2013).
[6] B. M. Wang, Y. Liu, P. Ren, B. Xia, K. B. Ruan, J. B. Yi, J. Ding, X. G. Li, and L. Wang, Phys. Rev. Lett. **106**, 077203 (2011).
[7] S. Chauhan, S. K. Srivastava, and R. Chandra, Appl. Phys. Lett. **103**, 042416 (2013).
[8] J. Saha and R. H. Victora, Phys. Rev. B **76**, 100405 (2007).
[9] T. Tohei, H. Wada, and T. Kanomata, J. Appl. Phys. **94**, 1800 (2003).

[10] K. Kamishima, T. Goto, H. Nakagawa, N. Miura, M. Ohashi, N. Mori, T. Sasaki, and T. Kanomata, Phys. Rev. B **63**, 024426 (2000).
[11] K. Asano, K. Koyama, and K. Takenaka, Appl. Phys. Lett. **92**, 161909 (2008).
[12] C. Wang, L. Chu, Q. Yao, Y. Sun, M. Wu, L. Ding, J. Yan, Y. Na, W. Tang, G. Li, Q. Huang, and J.W. Lynn, Phys. Rev. B **85**, 220103 (2012).
[13] S. Iikubo, K. Kodama, K. Takenaka, H. Takagi, and S. Shamoto, Phys. Rev. B **77**, 020409(R) (2008).
[14] K. W. Shi, Y. Sun, J. Yan, S. H. Deng, L. Wang, P. W. Hu, H. Q. Lu, M. I. Malik, H. Wu, Q. Z. Huang, and C. Wang, Adv. Mater. **28**, 3761 (2016).
[15] J. C. Lin, P. Tong, D. P. Cui, C. Yang, S. Lin, W. J. Lu, B. S. Wang, B. C. Zhao, and Y. P. Sun, Phys. Status Solidi B **252**, 582 (2015).
[16] W. Kuch, L. I. Chelaru, F. Offi, J. Wang, M. Kotsugi, and J. Kirschner, Nat. Mater. **5**, 128 (2006).
[17] E. V. Shevchenko, M. I. Bodnarchuk, M. V. Kovalenko, D. V. Talapin, R. K. Smith, S. Aloni, W. Heiss, and A. P. Alivisatos, Adv. Mater. **20**, 4323 (2008).
[18] See Supplemental Material at http://link.aps.org/supplemental/10.1103/PhysRevMaterials.3.024409 for details of the structural parameters.
[19] D. Niebieskikwiat and M. B. Salamon, Phys. Rev. B **72**, 174422 (2005).
[20] J. M. Perez-Mato, S. V. Gallego, E. S. Tasci, L. Elcoro, G. de la Flor, and M. I. Aroyo, Annu. Rev. Mater. Res. **45**, 217 (2015).
[21] D. Fruchart and E. F. Bertaut, J. Phys. Soc. Jpn. **44**, 781 (1978).
[22] P. Lukashev, R. F. Sabirianov, and K. Belashchenko, Phys. Rev. B **78**, 184414 (2008).
[23] Y. Sun, C. Wang, Y. C. Wen, L. H. Chu, M. Nie, and F. S. Liu, J. Am. Ceram. Soc. **93**, 650 (2010).
[24] S. H. Deng, Y. Sun, H. Wu, Q. Z. Huang, J. Yan, K. W. Shi, M. I. Malik, H. Q. Lu, L. Wang, R. J. Huang, L. F. Li, and C. Wang, Chem. Mater. **27**, 2495 (2015).
[25] J. Nogués and I. K. Schuller, J. Magn. Magn. Mater. **192**, 203 (1999).
[26] L. Szunyogh, B. Lazarovits, L. Udvardi, J. Jackson, and U. Nowak, Phys. Rev. B **79**, 020403(R) (2009).
[27] N. J. Gökemeijer, R. L. Penn, D. R. Veblen, and C. L. Chien, Phys. Rev. B **63**, 174422 (2001).
[28] V. K. Valev, M. Gruyters, A. Kirilyuk, and T. Rasing, Phys. Rev. Lett. **96**, 067206 (2006).
[29] Y. Shiratsuchi, H. Noutomi, H. Oikawa, T. Nakamura, M. Suzuki, T. Fujita, K. Arakawa, Y. Takechi, H. Mori, T. Kinoshita, M. Yamamoto, and R. Nakatani, Phys. Rev. Lett. **109**, 077202 (2012).
[30] Y. Du, G. Pan, R. Moate, H. Ohldag, A. Kovacs, and A. Kohn, Appl. Phys. Lett. **96**, 222503 (2010).